Engineering Geology 334 (2024) 107506

Contents lists available at ScienceDirect

Engineering Geology

journal homepage: www.elsevier.com/locate/enggeo

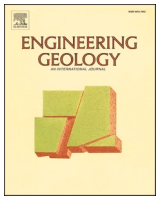

Practical considerations for using petrophysics and geoelectrical methods on clay rich landslides

James P. Boyd [a,b,*], Andrew Binley [b], Paul Wilkinson [a], Jessica Holmes [c], Edward Bruce [a], Jonathan Chambers [a]

[a] British Geological Survey, Keyworth, Nottingham, UK
[b] Lancaster University, Lancaster, UK
[c] Newcastle University, Newcastle, UK

ARTICLE INFO

Keywords:
Landslides
Geophysics
Petrophysics
Geoelectrical monitoring

ABSTRACT

Understanding the geological and hydrological conditions present within an unstable slope is crucial for assessing the likelihood of failure. Recently, geoelectrical characterization and monitoring of landslides has become increasingly prevalent in this context, due to the spatial sensitivity of electrical methods to critical hydro-mechanical parameters. We explore a situational relationship between resistivity and matric potential (or negative pore pressure), which is a key parameter in estimating the resistance to shear in geological materials, and gravimetric moisture content (GMC). We have chosen a well-characterized active landslide instrumented with geoelectrical monitoring technology, the Hollin Hill Landslide Observatory, situated in Lias rocks in the southern Howardian Hills, United Kingdom. We report on petrophysical relationships between porosity, GMC, electrical resistivity, and matric potential. We trial the application of these petrophysical relationships to inverted resistivity images. Ground model development is achieved through a mixture of clustering resistivity distributions and analysis of surface movements. Our findings show the shrink swell properties of clay result in a variable porosity, which is problematic for applying classic petrophysical relationships documented in the literature. Moreover, directly translating resistivity distributions into matric potential has additional challenges. Nonetheless, volumetric imaging of resistivity suggest that low shear strengths are concentrated downslope of a rotational backscarp. We infer that an accumulation of moisture drives the development of a slip surface at depth, which subsequently manifests in failure at the ground surface. We conclude that the time-lapse resistivity images alone could not be used to infer the pore pressure conditions present within the slope without development of the petrophysical relationships shown here. Therefore, we suggest that the results have practical implications for landslide monitoring with geophysical methods.

1. Introduction

Landslides have detrimental impacts on infrastructure and society, often associated with loss of life and substantial socioeconomic impacts (Gibson et al., 2013; Haque et al., 2019; Ozturk et al., 2022). To mitigate the risk posed by landslides, an understanding of the geomechanical and hydrological conditions within a slope that contribute to slope failure is necessary. Moisture induced slope failures associated with rainfall infiltration, are becoming more widespread and frequent in parts of the world susceptible to climate change (Fischer and Knutti, 2016). Here we build on recent studies investigating the use of long-term geoelectrical monitoring to characterize unstable hillslopes and hydrological processes occurring within a slope (Whiteley et al., 2019). A key advantage of geophysical methods over conventional techniques, including remote sensing and intrusive investigations, is that they are spatially sensitive to subsurface properties, rather than providing information about the ground surface or discrete locations at depth. Electrical resistivity tomography (ERT, also known as electrical resistivity imaging) is sensitive to the lithology, texture, pore fluid saturation, pore fluid resistivity, porosity, and temperature of rocks and soils. Therefore, in the absence in any change to the geology (bedrock or superficial), temporal variation in resistivity can be attributed to changes in the subsurface pore fluid resistivity and saturation, as well as ground temperature. Slope stability is influenced by the shear strength

* Corresponding author at: British Geological Survey, William Smith Building, Nicker Hill, Keyworth, Nottingham NG12 5GG, UK.
E-mail address: jamyd91@bgs.ac.uk (J.P. Boyd).

https://doi.org/10.1016/j.enggeo.2024.107506
Received 9 October 2023; Received in revised form 9 February 2024; Accepted 11 April 2024
Available online 13 April 2024

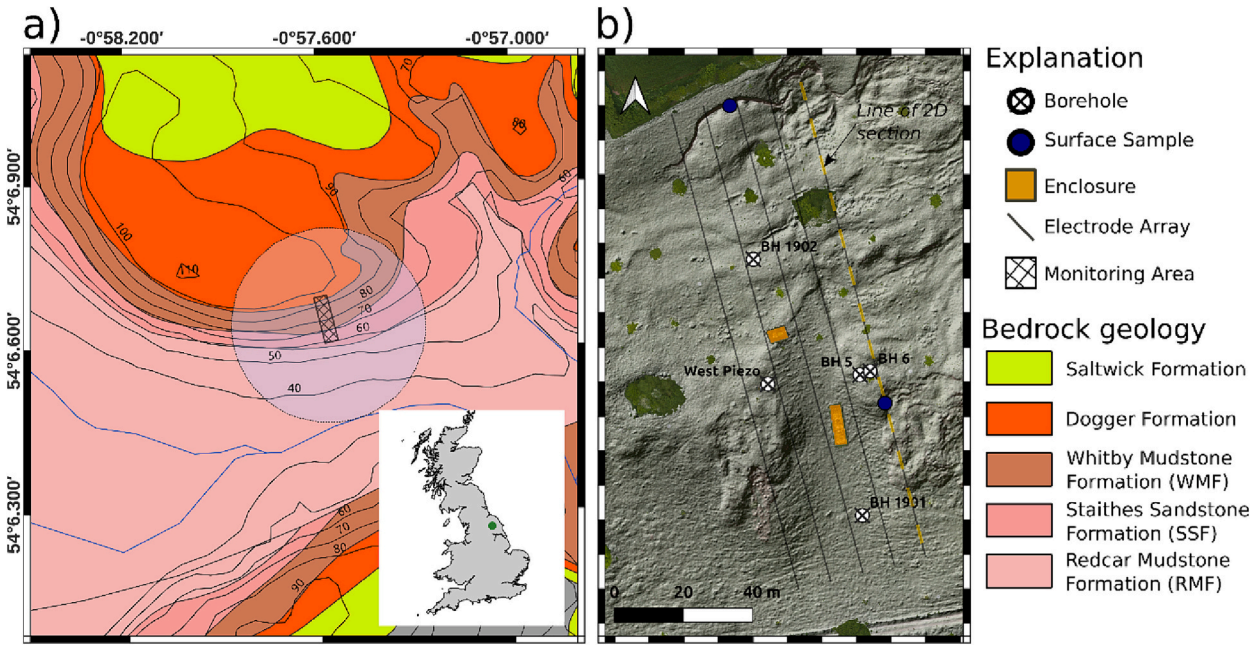

Fig. 1. a) Map showing the local geology according to regional geology maps, location of monitoring array and approximate sensitivity area of the moisture content sensor instrumentation (Zreda et al., 2008). Inset map shows location of field site (green dot) in the UK b) Overview of the monitoring array, sampling locations, boreholes, and equipment enclosures. The hill shade map (and aerial imagery) is modified from Peppa et al. (2019). (For interpretation of the references to colour in this figure legend, the reader is referred to the web version of this article.)

within a slope. In unsaturated conditions, pore saturation provides a critical control on negative pore pressure (or matric potential, or soil suction), which contributes to unsaturated shear strength (Bishop, 1959; Fredlund et al., 1996; Lu and Likos, 2006; Vanapalli et al., 1996). Whereas, in saturated conditions, pore pressure is predominantly a function of depth below the water table. Functions relating electrical resistivity to rock and soil saturation have long been established (Archie, 1947; Glover et al., 2000; Waxman and Smits, 1968); by extension this implies that resistivity could be used to infer the likely matric potential conditions within a slope (Cardoso and Dias, 2017; Crawford and Bryson, 2018; Hen-Jones et al., 2017; Piegari and Di Maio, 2013).

Geophysical methods are increasingly being used as hydrological monitoring tools (Binley and Slater, 2020) and workflows are being developed to relate electrical resistivity to hydrological parameters, including hydraulic conductivity and unsaturated soil retention properties (Johnson et al., 2017; Mboh et al., 2012; Pleasants et al., 2022; Tso et al., 2020). The sensitivity of electrical resistivity (or its inverse, electrical conductivity) to moisture content has been a key driver in developing long-term geophysical monitoring solutions. Regarding landslides specifically, Uhlemann et al. (2017) demonstrated, through a petrophysical transfer function and knowledge of soil particle density, that a time series of inverted electrical resistivity models can be converted into gravimetric moisture content (GMC) models. It was found that elevated moisture contents were associated with slope movements. The methodology of Uhlemann et al. (2017) was applied at the Hollin Hill Landslide Observatory (HHLO), the same field site investigated in this study.

Few authors have attempted to measure both matric potential and electrical resistivity in the laboratory (Cardoso and Dias, 2017; De Vita et al., 2012; Holmes et al., 2022) and in general show the two properties are related by an S shaped curve. Piegari and Di Maio (2013) described one of the first such instances of relating electrical resistivity and matric potential in the field, translating 3D resistivity volumes into matric potential for unstable slopes dominated by pyroclastic soils. Crawford and Bryson (2018) showed that electrical resistivity could be related to matric potential through calibration of in situ sensors placed within a landslide and resistivities sampled from ERT models. These potentials were then converted into a shear strength estimate using appropriate parameters from geotechnical testing. Holmes et al. (2020) also observed a relationship between electrical resistivity and matric potential by calibrating in situ sensors with inverted resistivity datasets in British Columbia, Canada. However, in this case there was the added complication that the hydrologically active layer at the field site froze during the winter period, during which the ground resistivity increased sharply even though the near surface material was saturated. More recently the same authors built on this study with laboratory-derived matric potential – resistivity relationships (Holmes et al., 2022).

1.1. Motivation and aims

While geophysical investigations of landslides are becoming more widespread, we contend that petrophysical relationships are required for geophysical measurements to be appreciated in an engineering context, be it as a precursor to coupled modeling (e.g. Camporese et al., 2015; Johnson et al., 2017; Pleasants et al., 2022; Tso et al., 2020), or used to provide a direct link between geophysical parameters (e.g. resistivity) and their hydro-mechanical counter parts. Therefore, we study petrophysical relationships between electrical resistivity, gravimetric moisture content (GMC) and matric potential. The relationships are applied to 3D volumetric resistivity images of a clay-rich slope, Hollin Hill. However, in the process of developing this work we encountered practical challenges to using such proxies. These include electrical anisotropy and shrink swell properties that we observed in the clay rich rocks present at Hollin Hill. Hence, we aim to document some practicalities of applying these relationships to field scale studies. Additionally, we hope to advance understanding of the hydrogeology of this specific field site.

2. Field site

Hollin Hill is located approximately 11.5 km west of the town of Malton in the UK county of North Yorkshire, in the southern part of the Howardian Hills. The HHLO is located within Lias Group rocks of the Lower Jurassic, which extends from the north eastern to southern coast

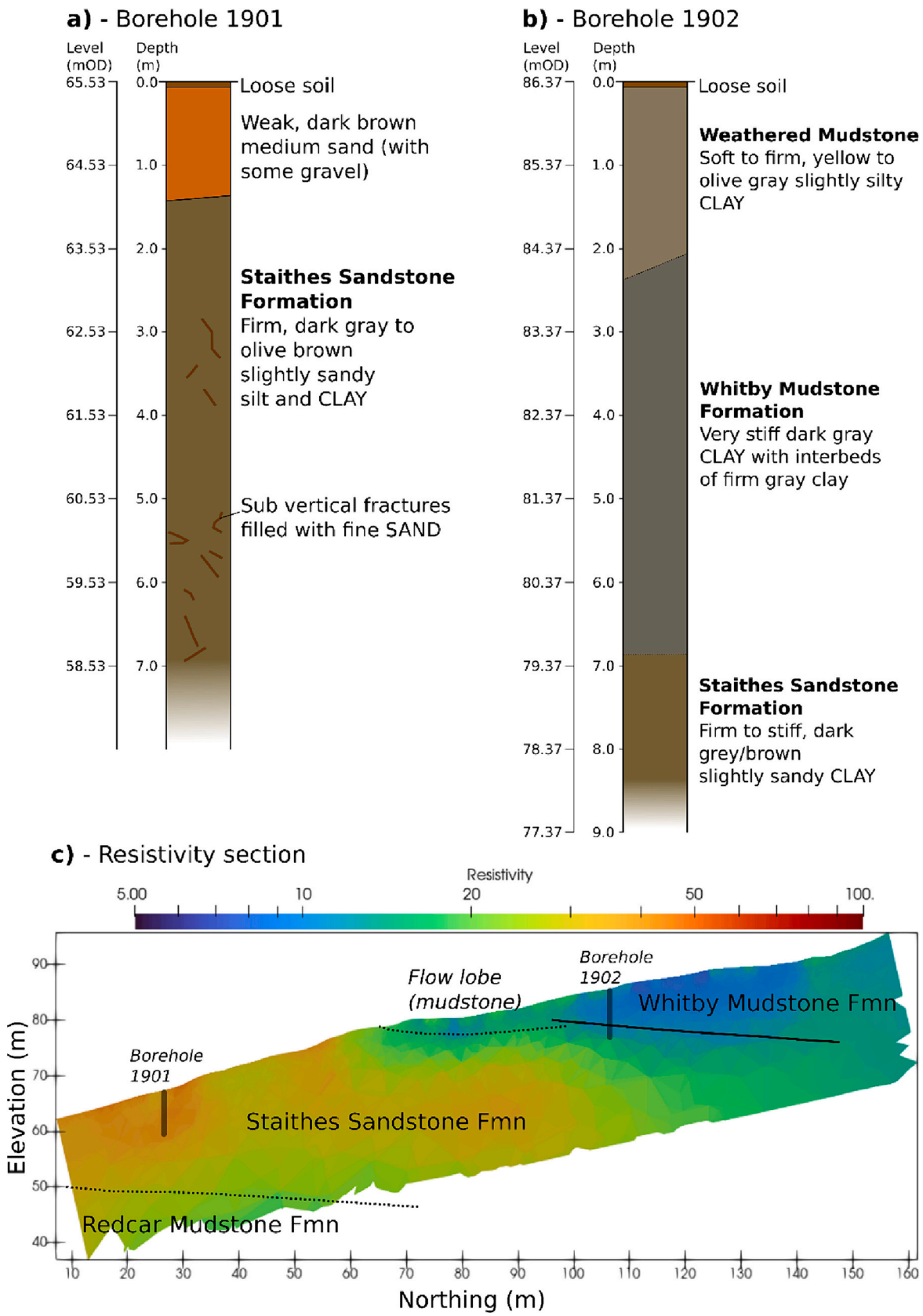

Fig. 2. a) Simplified interpretation of core (and geophysical logs) collected at borehole 1901, b) simplified log for borehole 1902, c) resistivity section with geological interpretation (positions indicated in Fig. 1).

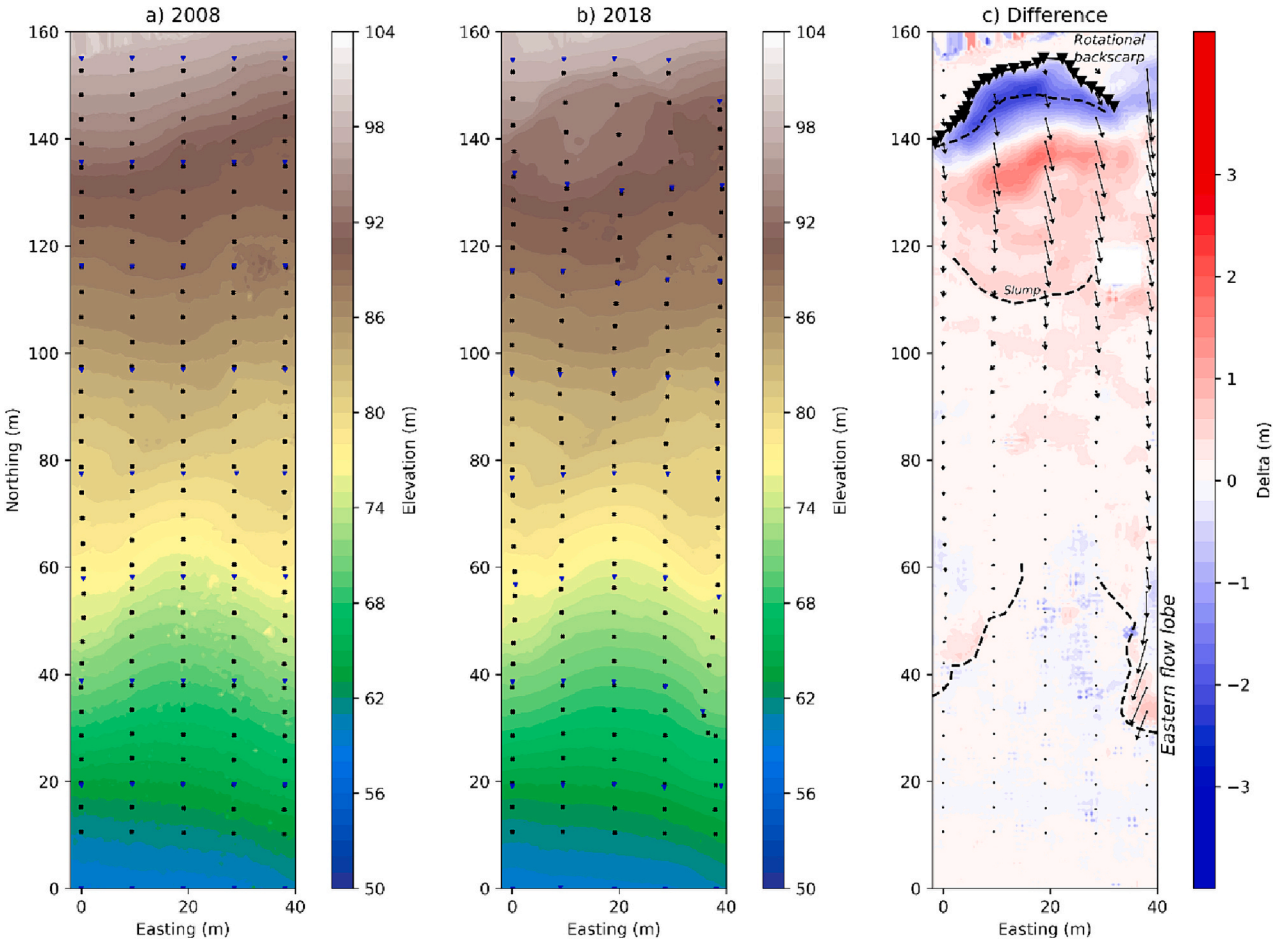

Fig. 3. a) Map of surface topography, marker pegs (blue triangles) and electrode placement (black dots) in 2008 after the ALERT (geoelectrical monitoring) system was first installed. b) Map of surface topography and electrode positions after nearly 10 years of monitoring. c) Colour map indicates whether the surface of the landslide has moved vertically, while arrows indicate the lateral movements of electrodes. Adapted from (Boyd et al., 2021a). (For interpretation of the references to colour in this figure legend, the reader is referred to the web version of this article.)

of the UK, and are widely associated with slope instability (Hobbs et al., 2005). To summarize the site geology; the Redcar Mudstone Formation (RMF) is located at the base of the sequence and is conformably overlain by the Staithes Sandstone Formation (SSF). The overlying WMF has a gradational contact with the SSF at its base and is capped by an erosional unconformity at its upper boundary. At the top the sequence is the Dogger Formation which outcrops outside of the study area to the north of the slope (Fig. 1).

In terms of the landslide failure processes, it is the WMF and SSF which are of the particular interest. Borehole geological records show the WMF is comprised of interbedded siltstones and mudstones, with evidence of ironstone beds towards its base that have been recorded elsewhere (Hobbs et al., 2005). The SSF found at this site largely comprises interbedded mudstones and siltstones, however borehole records indicate numerous sandy filled fractures and horizons. The Dogger Formation outcrops above the head of the landslide. According to the nomenclature of Varnes (1978), the landslide can be described as a complex slow moving flow. Surface movements suggest two major modes of failure: plastic deformation is observed on lobes of disturbed WMF material located downslope of a central terrace, and rotational failures are observed at the head of the landslide which expose weathered bedrock surfaces (Fig. 1). The main backscarp, characterized by rotational failures, is seated in WMF bedrock. Between the backscarp and mid slope limit of in-situ WMF the landslide develops into a zone of translational movement, which in the lower section of the slope transitions into an earthflow dominated regime overriding the SSF and RMF. Relict and eroded older earthflows, or colluvium, are present at the base of the slope and extend, in places, onto the valley floor. All the landslide material observed at site is derived from the WMF.

The HHLO has been characterized through several geotechnical, geomorphological and geophysical studies (Boyd et al., 2021a, 2021b; Chambers et al., 2011; Dixon et al., 2010; Gunn et al., 2013; Merritt et al., 2013; Merritt et al., 2018; Merritt et al., 2016; Peppa et al., 2019; Uhlemann et al., 2017; Uhlemann et al., 2016; Uhlemann et al., 2015; Whiteley et al., 2020). Fig. 1 shows the position of Hollin Hill with respect to regional geology and the setup of monitoring instrumentation. The interpretation of the slope resistivity distribution presented in Fig. 2 has been constructed using ERT, seismic refraction tomography (SRT), borehole investigations (Fig. 2) and geomorphological mapping. Particularly, boreholes denoted 1901 and 1902, retrieved in July of 2019, have been critical to this study (Fig. 1, Fig. 2).

2.1. Instrumentation

After initial geotechnical and geophysical investigations, Hollin Hill was established as a permanent landslide observatory (Boyd et al., 2021a; Merritt et al., 2018; Uhlemann et al., 2017). In particular, an automated time-lapse electrical resistivity tomography (ALERT) monitoring system (Kuras et al., 2009; Ogilvy et al., 2009) was installed in 2008, with arrays of electrodes positioned from above the head to beyond the toe, extending across the head scarp and two separate flow lobes (Fig. 1). The monitoring arrays comprised five lines, each with 32

electrodes buried at 0.1 m depth. At the time of installation, the along-line spacing of the electrodes was 4.75 m and the spacing between lines was 9.5 m (Fig. 1). This array geometry allowed for a predicted depth of investigation to 10s of meters and provided good overall coverage given the maximum number of electrode channels addressed by ALERT (160). An enclosure in the centre of the array hosted the ALERT measurement instrumentation, 3G/4G wireless router, batteries, and solar panels. The system ran almost continuously from March 2008 to September 2018, being replaced by a successor ERT monitoring system in October 2020.

An additional monitoring station was constructed in March 2014 to house a state-of-the-art weather station and COsmic-ray Soil Moisture Observing System (COSMOS) (Zreda et al., 2012) between arrays 3 and 4 (Fig. 1 b). The COSMOS instrument measures the number of neutrons generated by cosmic rays in the air and soil. As hydrogen atoms moderate neutrons, the number of neutrons emitted by soil can be measured to yield an estimate of volumetric moisture content (VMC) Zreda et al. (2008). The system is sensitive to soil moisture up to 76 cm below the ground surface in a circular area of approximately 330 m radius (Fig. 2) (Zreda et al., 2012).

Conceptual understanding of the HHLO is supported by a suite of more conventional sensors; alongside the resistivity monitoring system are thermometers, tilt meters, piezometers and shape acceleration arrays (SAAs). These clusters of sensors are placed in shallow boreholes on the two earthflow lobes in the eastern and western flanks of the monitoring area (Fig. 1). A shallow borehole with thermistors was used to a create a seasonal temperature depth model to offset changes in ground resistivity due to temperature (Uhlemann et al., 2017). In order to capture any electrode movements a sparse grid of marker pegs was installed at the surface which were then periodically surveyed with an RTK-GPS (real time kinematic global positioning system) to record any movements (Boyd et al., 2021a; Uhlemann et al., 2015).

2.2. Slope movements

The site comprises a combination of active and relict landslide features, with evidence of slope instability occurring since the last glaciation in the Pleistocene (Uhlemann et al., 2017). Since the commencement of geophysical monitoring, significant geomorphic changes have occurred due to slope movements. Peg coordinate data indicate where these movements occurred (Fig. 3) inside the 160 by 40 m monitoring area. There are two flow lobes where, month duration, meter scale movements downslope were recorded in 2008, 2009 and 2012 after periods of increased rainfall (Uhlemann et al., 2017; Wilkinson et al., 2010).

In April 2016, a backscarp resulting from rotational movement developed at the head of the landslide (Fig. 3). Initial field observations showed the exposed backscarp to be 1 m high and exposed weathered WMF. This feature has continued to grow and dominates failure processes of the upper part of the slope. As of 2023 the backscarp is >3 m high in parts and approximately 30 m across (Fig. 3). A slump which is characterized by translational movement developed downslope of the backscarp to accommodate these movements.

Slope movements have disturbed the natural structure of the geological formations. From here on in when reference is made to "disturbed material" this is material which has been either weathered or reworked by slope movements (not by retrieval for analysis), core logs suggest this extends to ~1.5 m below ground level. "In-situ material" is material which does appear to be affected by slope movements.

2.3. Hydrogeology

The upper part of the slope is composed of the WMF, which is a clay-rich material; particle size analysis (PSA) shows that up to 69% of flow lobe material is clay and 29% silt. The material is considered to have a low hydraulic conductivity of ~0.01 m.day^{-1} (van Woerden et al., 2014); however, the surface of the landslide is heavily fissured due to shrink-swell processes and progressive deformation of the slope. Piezometric data and geophysical studies indicate that the WMF hosts a perched water table (Gunn et al., 2013; Merritt et al., 2018; Uhlemann et al., 2017), with high saturation levels observed in the flow lobes during the winter months and sag ponds below the back-scarp in the upper part of the slope. Additionally, 2D high-resolution seismic sections of the slope (Whiteley et al., 2020) show a high wave speed band occurs in the WMF, although it is unclear whether this can be attributed to ironstone beds reported to be present at the base of the WMF (Hobbs et al., 2005) or if it relates to a water table. Furthermore, Boyd et al., 2021a found that the resistivity below the outcrop of WMF was relatively constant over 8 and a half years of monitoring compared to the rest of the geophysical model, suggesting that if the material is fully saturated, and remains so throughout seasonal cycles.

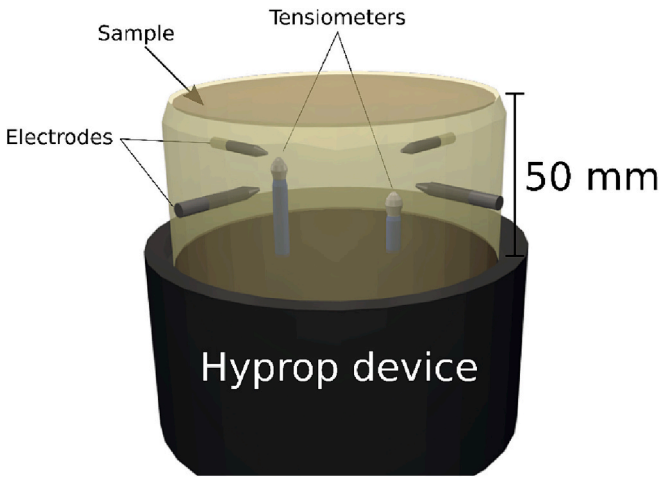

Fig. 4. 3D illustration of the experimental setup used to determine moisture content, electrical resistivity, and matric potential relationships. The HYPROP 2 device is connected to a data logger via a universal serial bus interface (which also provides power). The measurements from the 4-point electrodes are logged separately.

The resistivity of the WMF is typically relatively low (<30 Ωm) in ERT models (Fig. 1), which is associated with high GMC and clay content (Uhlemann et al., 2017). The flow lobes of WMF drain into the SSF during the summer and autumn months, and hence experience a large range of saturations throughout seasonal cycles, which is demonstrated by a large temporal range of resistivities (Boyd et al., 2021a). On the other hand, the SSF is comparatively more permeable, and the sand filled fractures present within the unit (Fig. 2) are likely to act as hydrogeological pathways (slug tests show that the hydraulic conductivity of the SSF is up to ~0.64 m.day^{-1}). ERT-derived GMC (Merritt et al., 2016; Uhlemann et al., 2017) shows the sandstone to have consistently lower moisture contents indicating water levels within the SSF are likely to reflect the regional ground water table, which intersects a tributary of the river Derwent (Ings Beck) south of Hollin Hill (Fig. 1). It is interesting to note that during periods of heavy rainfall, natural springs develop at the base of the SSF on the interface with the underlying RMF.

3. Methodologies

The scope of this study focuses on petrophysical relationships between matric potential, resistivity, and GMC (gravimetric moisture content). Here we consider the methodology used to establish petrophysical relationships, the processing of geoelectrical data from the field site (Hollin Hill specifically) and the incorporation of the petrophysical relationships into a dynamic geophysical model of the slope with a slip surface. The results corresponding to the petrophysical relationships merit their own section will be revisited.

3.1. Resistivity and matric potential

We study an empirical relationship between the electrical conductivity of the material and its respective matric potentials in the laboratory. Electrical conductivity, soil tension and GMC are measured using a modified HYPROP 2 device (Fig. 4) from METER Group. The samples are contained in a density ring made of a hard polymer. Samples are collected from either borehole core (1901, 1902) or from shallow pits.

3.1.1. Petrophysical theory

Measurements between the electrical resistivity and matric potential are observed directly. These measurements can be fitted with an "S shape" curve, supporting prior studies where there is an empirical relationship between resistivity and pressure in unsaturated conditions (Cardoso and Dias, 2017; Crawford and Bryson, 2018; De Vita et al., 2012). Conceptually, we propose why such curves can replicate the observations. The saturation conditions within a clay-rich material can be described as one of three states: saturated, partially saturated and residual. In the saturated state, the electrically conductive double layer and pore fluid both contribute to conduction in the clay, while in the partially saturated state the contribution of the pore fluid is reduced due to air (an electrical insulator) partially occupying pores. In the residual state electrical conduction is largely dominated by conductivity of the clay as the movement of ions in residual pore fluid is restricted due to isolated pores. Consequently, we can treat electrical conductivity the same as a saturation value in, for example, a van Genuchten (1980) moisture retention curve; hence curve parameters are fitted to a relative conductivity,

$$EC_{norm} = \frac{EC_{meas} - EC_{res}}{EC_{sat} - EC_{res}} \quad (1)$$

where EC_{sat} and EC_{res} are the relative electrical conductivity at saturated and residual conditions, respectively. Note that electrical conductivity is the inverse of resistivity. Following the suggestion by Crawford and Bryson (2018) and others (Cardoso and Dias, 2017), matric potential can then be related to electrical conductivity in a relationship that has the same form as that of van Genuchten (1980) for a relative saturation – soil suction curve, i.e.:

$$EC_{norm} = (1 + [\alpha h]^n)^{-m} \quad (2)$$

where α and n are functionally equivalent to van Genuchten fitting parameters, h is the matric potential, and here we adopt common assumption that $m = 1 - {}^1/_n$. Unless the relationship between normalized conductivity and moisture content (or degree of saturation) is linear (Crawford and Bryson, 2018), which is unlikely for most geological materials, α and n do not have the same physical meaning as when expressing van Genuchten's relationship in terms of degree of saturation. This conceptualisation describes a mechanism whereby electrical conductivity derived from ERT measurements can be used to estimate potentials in the unsaturated portion of the near surface. In saturated conditions (below the water table) the electrical conductivity should not be used as a proxy for pore pressure because the changes in electrical conductivity will be driven by other processes, such as pore fluid composition.

3.1.2. Experimental setup

The experimental setup of our modified HYPROP system is also described by Holmes et al. (2022). In summary, the setup comprises a cylindrical sample placed on a digital balance, in a temperature-controlled laboratory (Fig. 4). Inserted into the sample are 4 electrodes (for a 4-point resistivity measurement) and two tensiometers (Fig. 4). To prepare the sample a hard plastic (polyether ether ketone, PEEK) density ring was used to house the sample of known density and saturated in deionized, de-aired, water; then the sample was transferred to the balance and left to dry at 20 °C. The density ring has a height and

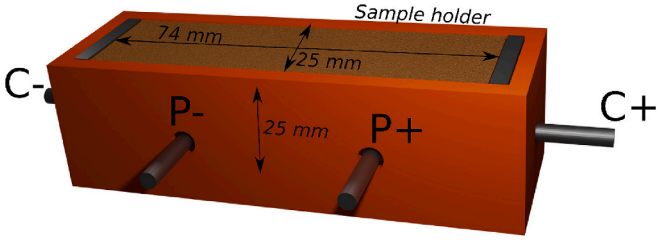

Fig. 5. 3D schematic of the sample holder used to test the resistivity – GMC relationship. Current electrodes are placed either end of the long axis of the sample.

radius of 50 mm (Fig. 4). The reason for using deionized water is to simulate rain which has a low electrical conductivity; furthermore once in the sample the pore fluid will entrain ions from the host rock. The resistivity of the sample, matric potential and sample weight were logged for the duration of the air-drying experiment. The two tensiometer measurements were averaged after the experiment to give an estimate of suction in the sample at various sample weights. When the tensiometer reached cavitation the recording of matric potential was stopped, however the experiments were continued until the sample conductivity started to reach an asymptote, to estimate resistivity at near-residual saturation.

Samples were selected to include the key lithologies (Fig. 1): two samples of WMF from the eastern flow lobe, in shallow pits, and one from the exposed back scarp area, and one from the SSF recovered from core. The density rings were driven into formations, vertically, using a mallet and a wooden plate (on top of the ring). Where shallow pits were used, samples were sealed at site to prevent moisture loss. Borehole core was also cased at site but broken open in the laboratory around the circumference of the casing such that density rings can be driven into the material. Unfortunately, the sample retrieved for the SSF cavitated (allowed air ingress) early in the experiment, hence we focus on matric potential – resistivity relationships for the WMF only. Notably the WMF is the most important formation regarding slope failure.

3.1.3. Curve fitting

The relationship between matric potential and the inverse of electrical resistivity is assumed to follow Eq. 2. In order to fit empirical models to our experimental results we used a Markov chain Monte Carlo (McMC) approach (Hastings, 1970). The motivation for this approach is that it can be used to find model parameters with some indication of parameter error bounds. The values of α, n and their respective error distributions were found by a Gaussian fit to their respective posterior

Table 1
Sample names, and their respective boreholes and retrieval depths. Borehole placements are shown in Fig. 1.

Sample Formation	Borehole	Depth (m)	Alignment	Material type
SSF	1901	1.50	Horizontal	Disturbed Staithes Sandstone
SSF	1901	1.50	Vertical	Disturbed Staithes Sandstone
WMF	1902	0.95	Horizontal	Weathered Whitby Mudstone
WMF	1902	1.05	Vertical	Weathered Whitby Mudstone
WMF	1902	3.00	Horizontal	In-situ Whitby Mudstone
WMF	1902	3.10	Vertical	In-situ Whitby Mudstone
WMF	1902	6.10	Horizontal	In-situ Whitby Mudstone
WMF	1902	6.20	Vertical	In-situ Whitby Mudstone

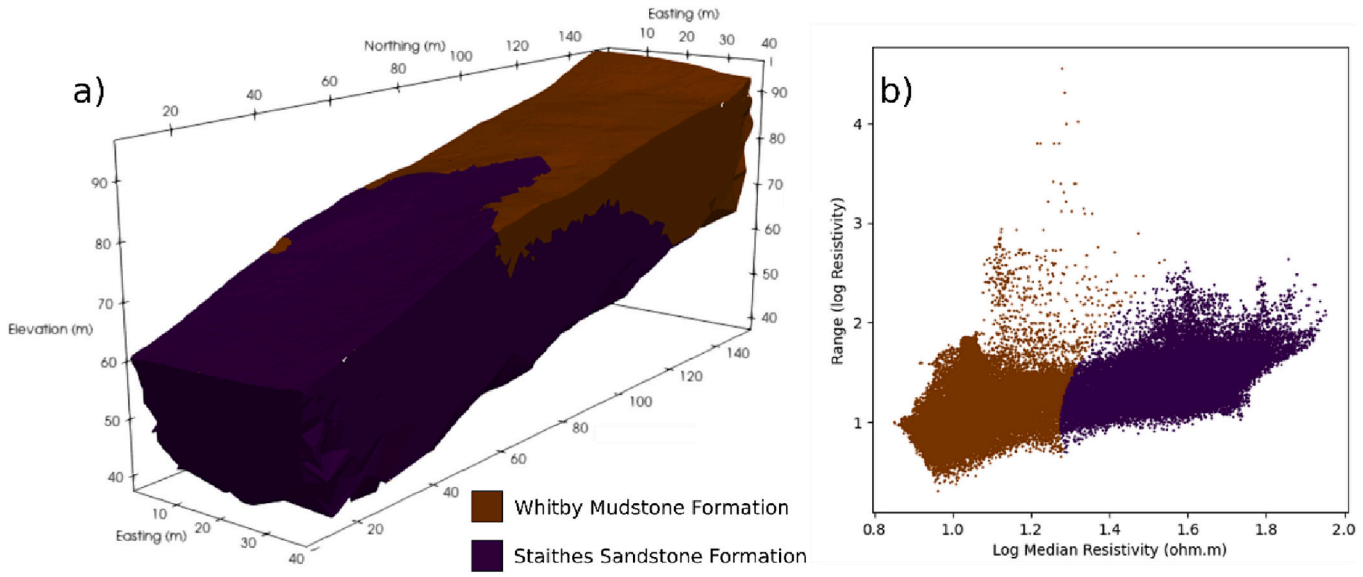

Fig. 6. a) Mapping of clustering to ERT model domain. b) A scatter plot of all resistivity values in the processed ERT domains, colors indicate relevant cluster.

probabilities identified in the McMC process, as the probability density functions appeared to follow a normal distribution.

3.2. Moisture content and resistivity relationships

In addition to the HYPROP experiments, some samples were retrieved for independent GMC and resistivity analysis to test electrical anisotropy (also in the laboratory). A previous study of Hollin Hill (Merritt et al., 2016) found that the electrical resistivity and GMC relationship can be anisotropic with respect to the orientation of bedding plains. Material was extracted from borehole core and placed into 3D printed sample holders (Fig. 5). Plate electrodes either side of the holder's long axis were used to orientate current flow direction with respect to bedding plains. Sample holder internal dimensions measured 25 by 25 by 74 mm. Two samples were extracted at each depth horizon of interest (Table 1) to sample the soil moisture - resistivity relationship in the horizontal and vertical axes of the borehole.

As in a prior study of Hollin Hill (Uhlemann et al., 2017), a relationship between resistivity and GMC, Θ_g, was fitted using a modified Waxman-Smits relationship (Chambers et al., 2014; Waxman and Smits, 1968):

$$R(\Theta_g) = F\left(\frac{(1-\Phi)p_g\Theta_g}{\Phi p_w}\right)^{-n}\left(\sigma_w + B_{ws}\left[\frac{(1-\Phi)p_g c_e}{100\Phi}\right]\left[\frac{\Phi p_w}{(1-\Phi)p_g\Theta_g}\right]\right)^{-1} \quad (3)$$

where R is rock resistivity, Φ is porosity (void fraction), σ_w is pore fluid conductivity, p_g is grain density and p_w is water density (assumed equal to 1 g.cm^{-3}), c_e is cation exchange capacity, B_{ws} represents the conductance of counterions and is calculated as a function of σ_w (Waxman and Smits, 1968), finally F is formation factor and n is the saturation exponent. The cation exchange capacity and pore fluid conductivity were previously determined by Merritt et al. (2016) for both the WMF and SSF, B_{ws} is calculated to take a value of 2.042 (S cm^3 m^{-1} meq^{-1}).

It was hypothesised that the shrink-swell properties of clay present would alter the porosity of the sample at various saturation levels as has been observed in other studies (Hen-Jones et al., 2017; Holmes et al., 2022; Merritt et al., 2016; Saneiyan et al., 2022), therefore in this case $\Phi = f(\Theta_g)$. The shrinkage curve of the materials from Hollin Hill was investigated (see Section 3.2.1). When computing GMC from resistivity a value for porosity is also estimated; it was found this additional step was necessary to achieve a reasonable fit with the data.

3.2.1. Sample porosity

Using a SHRINKiT system (Hobbs et al., 2010) the mass and volume of field samples were measured as they dried. This showed that the volume of samples decreased until their shrinkage limit, approximately 10% GMC, as they dried. At the end of the experiment the samples were oven dried at 105 °C to give a final dry mass from which gravimetric moisture content (GMC) could be estimated. Additionally, the grain density of the WMF was established through particle size analysis (2.74 g.cm^{-3}), hence the porosity of the sample could be estimated as a function of GMC. Porosity can be computed as,

$$\Phi = \frac{V_i - \left(\frac{M_d}{p_g}\right)}{V_i}, \quad (4)$$

where V_i is the sample volume at a given time in the SHRINKiT experiment, and M_d is the dry mass of the sample (g). GMC can be related to porosity following the approach of Peng and Horn (2005),

$$\Phi\left(\Theta_g\right) = \Phi_r + \frac{\Phi_s - \Phi_r}{\left[1 + \left(\frac{\alpha_{ph}\cdot\Theta_g}{\Phi_s - \Theta_g}\right)^{-n_{ph}}\right]^{m_{ph}}}, \quad (5)$$

where Φ_r and Φ_s are the porosity at residual saturation and fully saturated conditions, respectively, α_{ph} and $n_{ph}$are fitting parameters and its assumed $m_{ph} = 1 - {}^{1}/_{n_{ph}}$.

3.3. ERT processing

We adopt a baseline-constrained approach similar to prior studies (Uhlemann et al., 2017; Whiteley et al., 2020) whereby the inversion is constrained against a reference inverted image (in this case, from April 2010). Electrode movements (Uhlemann et al., 2015) and subtle changes in topography (Boyd et al., 2021a, 2021b; Whiteley et al., 2020) can cause artefacts in resulting time-lapse geoelectrical inversions that could be attributed to hydrological changes. Therefore, distortions to the slope surface are modelled with a series of thin-plate splines, interpolated from the displacements measured on each peg position, to produce a time-lapse series of digital elevation model (DEM) surfaces and electrode positions. The time-lapse surface of the DEM is periodically calibrated by either unmanned aerial vehicle (UAV) or terrestrial light detection and ranging (LiDAR) scans.

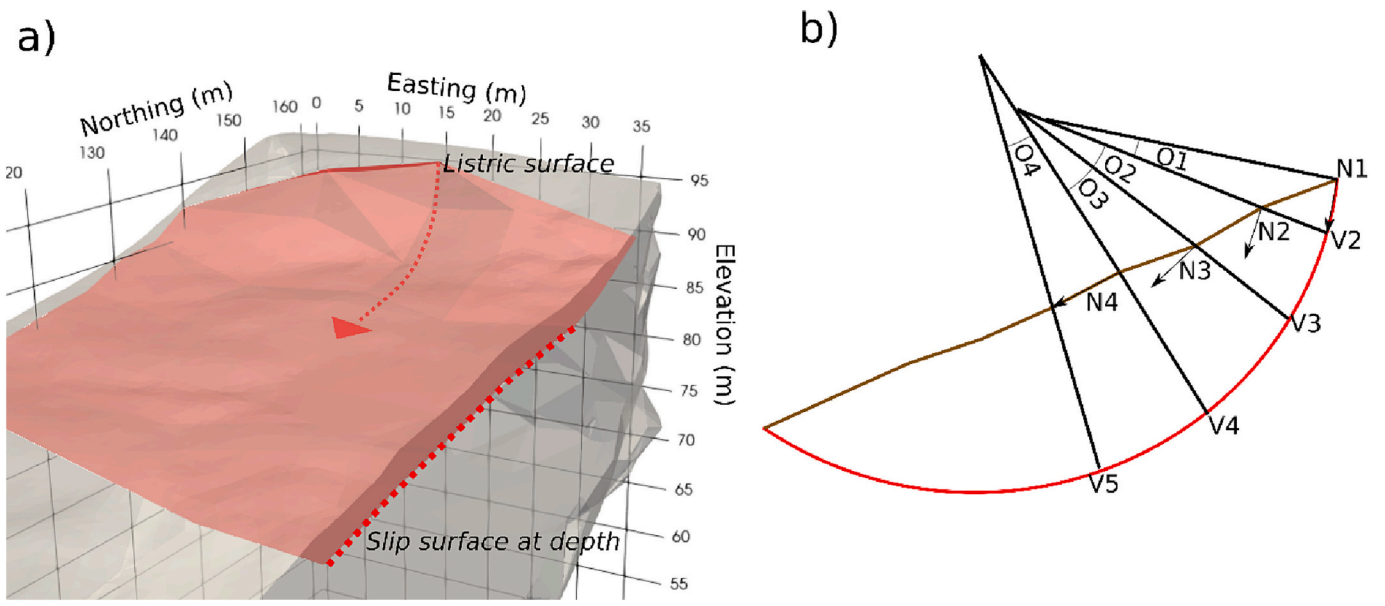

Fig. 7. a) Modelled slip surface inside the ERT modeling domain. b) Graphical representation of the Carter and Bentley method to determine the slip surface geometry.

ERT data quality varies throughout the monitoring period; degradation of the monitoring setup contributes to a general decline in quality metrics due to cable breakages (often caused be slope movements), loss of power and other malfunctions. Additionally, the drier conditions during the summer months results in elevated contact resistances and hence noisier and poorer quality data. As a pre-processing step, the raw transfer resistances collected by the ALERT system were filtered to remove measurements that had: a contact resistance over 5 kΩ; an approximate apparent resistivity outside the range of 0 and 200 Ωm (as apparent resistivities higher than this tended to be erroneous and the site is relatively conductive); a reciprocal error over 10%, or no reciprocal measurement. During the inversion, the transfer resistance (TR) data were weighted according to an error model which was formed by fitting a power law against binned data on a per survey basis (Binley and Slater, 2020). The TR data sets were prepared using ResIPy (Blanchy et al., 2019) and inverted using E4D (Johnson et al., 2010). A unique error model (Tso et al., 2017) was calculated for each survey date due to the different error properties associated with individual surveys and seasons. In order to calibrate the time-lapse resistivity models against seasonal ground temperature variations, the resistivity of each cell was corrected to a constant temperature (20 °C) using a ground temperature model and assuming a linear relationship between electrical conductivity and temperature (Uhlemann et al., 2017).

3.4. Ground model

To apply any petrophysical relationships to the inverted resistivity models from ERT measurements, the dominant lithologies inside the modeling domain need to be identified. Previous studies have used seismic methods to identify the boundary between the WMF and SSF (Uhlemann et al., 2016). Here we exploit the time-lapse component of the ERT-derived resistivity images to interrogate the range and median values of resistivity on a representative domain. Because resistivity can change by an order of magnitude between lithologies, clustering was performed in log space and was able to closely delineate the boundary between the WMF and SFF documented in previous studies (Uhlemann et al., 2016; Whiteley et al., 2020). A Gaussian mixture clustering algorithm (Pedregosa et al., 2011) was used allowing for two clusters, one for each dominant lithology (Fig. 6). The two lithologies were mapped to the inversion mesh (Fig. 6 b). Due to the changing topography of the site through the years, a different inversion mesh was used for each time step in the inversion process (Boyd et al., 2021a), hence a nearest neighbor lookup was used to map lithologies to subsequent time-lapse volumes. Distinct petrophysical transformations were applied depending on whether an individual mesh cell was identified as part of the SSF or WMF. Cells in the upper 1 m of the WMF domain were assigned petrophysical parameters based on the results of measurements made on disturbed samples reworked by slope movements and weathering.

3.5. Slip surface

Here the interest is in comparing the geophysical/petrophysical results with the predicted slip surface location in the upper part of the slope where rotational and translational failure is observed. Various authors, over the years, have proposed methods to recover the slip surface at depth from surface displacements. Efforts to model slip surface geometry have gained growing interest in recent years as remote sensing methods have facilitated displacement monitoring of large and remote landslides (Aryal et al., 2015; Booth et al., 2020). However, the most challenging aspect of modeling displacements is to identify collocated points on the slipped mass before and after movements. Given that interpolating electrode displacements is necessary for accurate ERT models, a 3D displacement field was produced as part of the ERT processing; hence we can adopt a relatively straightforward workflow to model the slip surface geometry at depth (Fig. 7), following the suggestions by Bishop (1999) and Carter and Bentley (1985). The former, known as the balanced cross section (BCS) method, assumes that the sliding mass retains its volume, before and after failure, therefore the depth to the slip surface is proportional to the displacement and total area lost at the landslide backscarp. However, the BCS method can only predict the depth of the main body of the landslide (or slipped mass), it does not describe the geometry of the listric surface (slip plane), in which case we adopt the latter suggestion (Carter and Bentley, 1985) to describe the geometry of the slip surface around the backscarp. The method can be described graphically, as in Fig. 7 b. In cross section view, for every displacement vector the normal, N_i, can be drawn above the landslide surface, where consecutive normal vectors intersect describes the centres of curvature, O_i, for the corresponding displacement pair. The resulting arcs can be used to inform the placement of the scarp surface vertices, V_i, where each arc intersects N_{i+1}. This method requires

Table 2
Fitted parameters found the porosity relationship. The 5th column shows the Pearson correlation coefficient between the data and fitted curve. N is the number of measurements used for curve fitting.

Φ_r	Φ_s	α_{ph}	n_{ph}	r	*N*	*Samples*
0.345	0.559	0.743 ± 0.005	2.730 ± 0.038	0.986	1495	4

that normal vectors emerging from the displacement field intersect above the landslide surface (so it best describes a rotational failure), in the case of Hollin Hill an inflection in surface displacements occurs such that the method is best suited to describing the listric surface only.

The depth to the slip surface is estimated for each profile of electrodes located in the slump and head areas of the landslide. The zone of depletion area is estimated along each profile by computing the difference in elevation for a series of thin (0.014 m wide) columns, while the displacement is taken as the maximum electrode displacement along each profile on the slump. The depth of the slip surface is then given as (Bishop, 1999),

$$H = A/D \tag{6}$$

where A is the depletion zone area and D is the measured displacement at the surface. To compute the geometry of the listric surface an iterative procedure was performed on the relevant electrode displacements, as

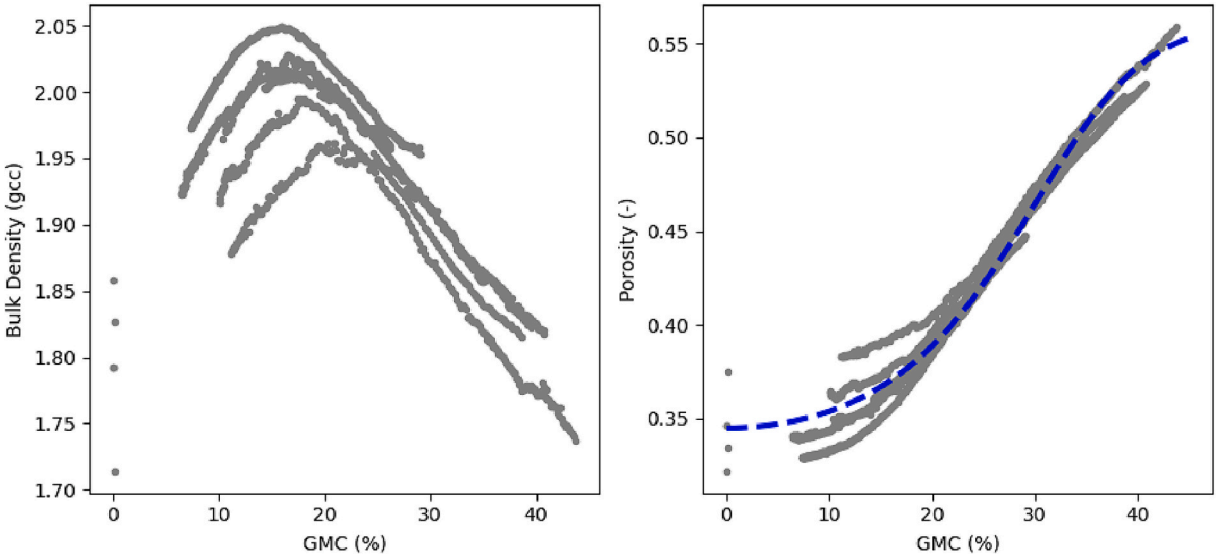

Fig. 8. Left, bulk density versus GMC (four different samples); right computed porosity versus GMC and fitted curve (blue dashed line). (For interpretation of the references to colour in this figure legend, the reader is referred to the web version of this article.)

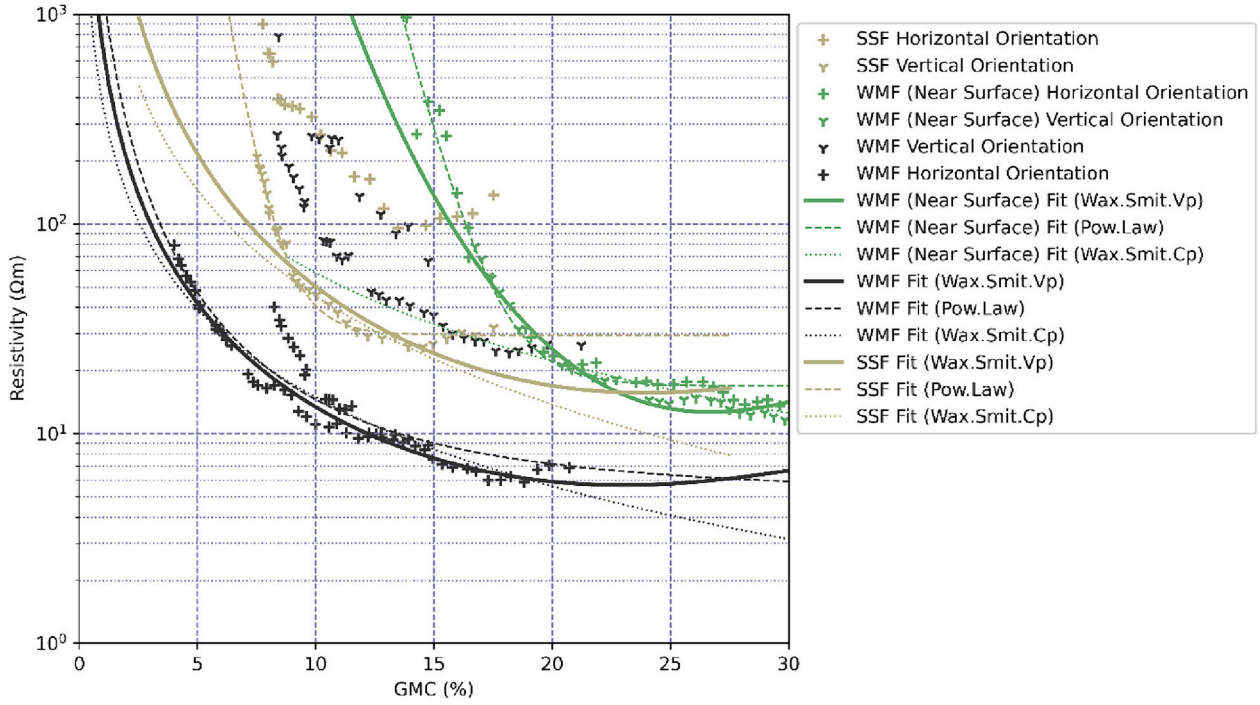

Fig. 9. Plot of GMC and resistivity and fitted curves. Explanation of sample names is included in Table 1. Regarding the legend and types of fit, the suffix 'Cp' stands for constant porosity and 'Vp' stands for variable porosity when using a Waxman-Smits curve.

Table 3
Parameters for the formations present at the Hollin Hill Landslide Observatory, WMF in-situ and disturbed and SSF. The 7th column shows the Pearson correlation coefficient between the fitted data and modelled resistivity values. Values with an error estimate are fitted through McMC curve fitting. N is the number of measurements used to fit the curves (and number of samples in backets).

Unit	F (m)	n (−)	p_g (gcc)	σ_w (s/m)	c_e(meq/100 g)	r	N
WMF (in-situ)	9.44 ± 0.39	2.74 ± 0.04	2.74	0.0987	22.5	0.95	66 (2)
WMF (dist.)	13.62 ± 0.37	10.06 ± 0.07	2.74	0.0987	22.5	0.91	66 (2)
SSF	12.44 ± 1.81	3.30 ± 0.39	2.74	0.0987	11.0	0.90	33 (1)

shown in Fig. 7 b. The 3D geometry of the rotational failure was developed by triangulating the depth to slip surface computed for each electrode profile (Fig. 7 a).

4. Petrophysical relationships

4.1. Porosity and GMC

A porosity – GMC relationship has been determined from samples retrieved from Hollin Hill, these include augured boreholes and shallow pits (boreholes 5, 6 and 'west piezo' locations indicated in Fig. 1). The fitting parameters in Eq. 5 are documented in Table 2 and shown in Fig. 8.

4.2. Resistivity and GMC

Samples retrieved from boreholes show anisotropy (Fig. 9) with respect to electrical current flow depending on the orientation of the sample. For the WMF the electrical resistivity is overall lower when electrical current flows parallel to bedding plains, suggesting ions preferentially migrate along bedding plains in the WMF. For the SSF electrical resistivity is lower when electrical current flow is perpendicular to bedding plains. Core logging showed macro-scale sand filled fractures perpendicular to bedding plains in the SSF, which suggests the fractures act as the preferential pathway for the migration of pore fluid in the SSF. We also recovered samples from 1 m below the ground surface in the WMF, which exhibit isotropy with respect to current flow, as there is no difference in magnitude of resistivity if the measurements are made parallel or perpendicular to bedding (Fig. 9). We observe that the disturbed material has been subject to plastic deformation and has lost its sedimentary textures and has become electrically isotropic. Differing trends for disturbed and in-situ samples show that different GMC – resistivity curves should be fitted to the data depending on whether the material has been disturbed by slope movements or is relatively undisturbed. Therefore, we fitted curves for shallow disturbed WMF material, deeper in-situ WMF material and SSF material (Tables 1 and 3, Fig. 9). For SSF samples, the vertically orientated sample showed lower resistivities compared to its horizontal counterpart. For anisotropic formations we fitted petrophysical relationships to trends which have lower resistivities, this is because the resistivity trends better match those observed in field ERT results (Fig. 1 b).

The saturation exponent of sedimentary material is typically close to 2 (Binley and Slater, 2020), without accounting for changes in porosity. Hence the n exponent for the disturbed WMF material is relatively high (~10, Table 3). We explored relationships proposed by Montaron (2009) as well but these did not provide as good a fit as Waxman-Smits model. Therefore, we adopted, a Waxman-Smits curve with a variable porosity for all lithologies studied here. We also found that an inverse power law with a variable asymptote is favourable in the case that variable porosity information was not available (Fig. 9), in which case resistivity is related

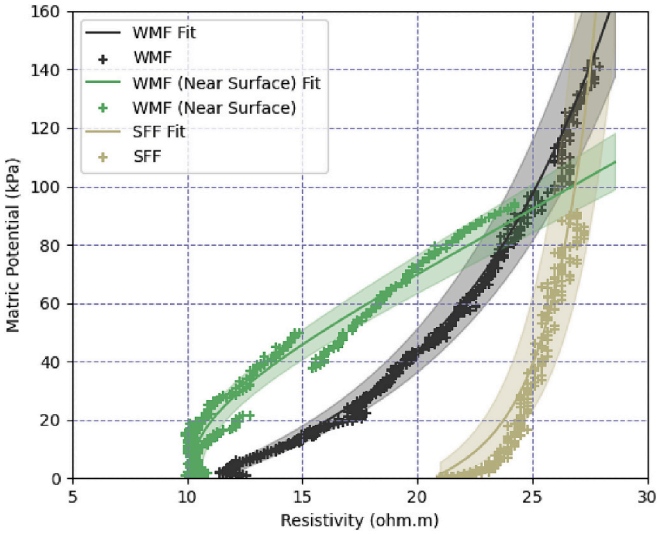

Fig. 10. Matric potential versus resistivity and fitted curves according to Eq. 2. Infilled regions indicate the extent of perturbing the error bounds of the fitted parameters in Table 4.

Table 4
Parameters for the WMF between resistivity and matric potential. Values with an error estimate are fitted parameters found with an McMC approach. The 6th column shows the Pearson correlation coefficient. N indicates the number of measurements.

Unit	E_s (mS/m)	E_r (mS/m)	α (−)	n (−)	r^2	N
WMF (insitu)	0.890 ± 0.037	0.166	0.114 ± 0.004	1.467 ± 0.007	0.997	705
WMF (dist.)	0.989 ± 0.042	0.067	0.024 ± 0.001	2.174 ± 0.011	0.965	549
SSF	0.482 ± 0.020	0.249	0.160 ± 0.006	1.227 ± 0.005	0.973	301

to GMC as

$$R(\Theta_g) = \frac{1}{a(\Theta_g^{\,b})} + c, \tag{7}$$

where a, b and c are fitting parameters. Indeed, we found that a generic power law worked well in the case of the SSF more so than the Waxman-Smits model with a variable porosity (Fig. 9).

4.3. Resistivity and Matric potential

The resistivity suction curve for the disturbed WMF samples retrieved from the flow lobe versus in-situ WMF were markedly different, hence, as with the moisture content relationships, we apply a different relationship for the disturbed and in-situ WMF (Table 4, Fig. 10). We used an McMC approach to fit the curve parameters shown in Eq. 2. However, we did observe a discrepancy in our inverted resistivity images and range of resistivities observed for our samples hence we revisit this relationship in the following section.

5. Petrophysical relationships in practice

As reported by other authors (Hen-Jones et al., 2017; Holmes et al., 2022; Saneiyan et al., 2022), the porosity influence on petrophysical relationships between resistivity and clay rich geological materials presents some challenges. For example, the formation factor (Archie, 1947; Waxman and Smits, 1968) is not constant under a variable porosity, hence the values of formation factor presented in this paper

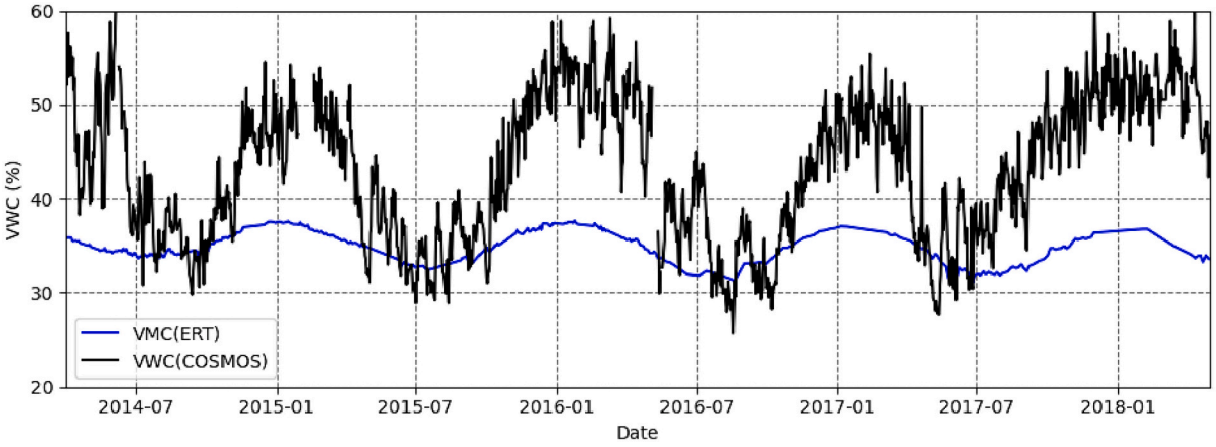

Fig. 11. Comparison of volumetric water content derived from the COSMOS instrument and that derived from time-lapse ERT by averaging resistivity values of the uppermost cells in the modeling volume at each time increment ERT survey data is available.

assume porosity varies as function of moisture content (Eq. 5). Prior studies of Hollin Hill did not account for variable porosities in their field petrophysical relationships (Uhlemann et al., 2017), as such this work represents an advancement in understanding this particular field site. The inclusion of variable porosity is necessary to achieve a reasonable fit between measurements and petrophysical model (in this case a modified Waxman-Smits curve). On the other hand, we also found that fitting a generic inverse power law with a variable asymptote worked well for fitting the data in the case that information about the variable porosity was unavailable, with the caveat that the fitted parameters have no physical meaning (such an approach could not account for differing pore fluid conductivities, for example).

Direct comparisons between saturation measured by in-field sensors and those derived by ERT have proven challenging due to different scales of investigation and interruptions and gaps in monitoring data. Many of the sensors installed at the HHLO developed faults during their lifetime and have not provided continuous measurement streams; the advantage of the COSMOS instrument at this field site is that it has been maintained since installation in 2014 and therefore has a four-year overlap with the ALERT data. The COSMOS data and ERT results both act as proxies for water content for a volume of the subsurface, and therefore both can be used to ground truth the petrophysical relationships explored in this study. To compare the time-lapse ERT results against the COSMOS data, the uppermost cells of the time-lapse resistivity meshes were isolated and averaged (Fig. 11), the approximate area covered is 5250 m^2. This is because the COSMOS instrument is assumed sensitive up to 76 cm depth for dry soils (12 cm for saturated soils) in an area 3.4×10^5 m^2 at sea level (Zreda et al., 2008). Fig. 11 shows some agreement between volumetric moisture content derived from the COSMOS sensor and the that derived from time-lapse resistivity (which can be computed via Eqs. 3–5).

The similarities between the COSMOS and ERT-derived moisture contents demonstrate that the ERT-derived moisture contents match the trends observed by the COSMOS station, and that ERT is sensitive to temporal variations in resistivity associated with different seasons (Fig. 11). Although we note that increases in VMC magnitude derived by ERT are vastly muted in comparison; a possible explanation for these differences is that the sensitivity pattern of the COSMOS weather station versus the ALERT system are different. The COSMOS system includes the entirety of the valley, which has a stream at its base and wetter valley sediments (Fig. 1), whereas ERT measurements are concentrated on a single slope.

The translation between electrical resistivity and matric potential appears to work well on laboratory samples, however issues arise when applying these relationships to field data. Both Holmes et al. (2022) and Crawford and Bryson (2018) report a discrepancy between their matric potential values predicted by petrophysical relationships and those that would be predicted by field ERT volumes (even when inverted images are temperature corrected). In this case we observe inverted resistivities which are lower than that observed by HYPROP measurements. The petrophysical relationship developed here was derived for a drying cycle; we suggest it is likely the WMF material would have a lower resistivity when wetting up versus drying as a result of hysteresis, which has been observed in other studies (Cardoso and Dias, 2017; Hen-Jones et al., 2017). More over any uncertainties arising from the sensitivity of the ERT method and temperature correction would be super imposed on matric potential predictions, particularly as both of these properties scale logarithmically. Piegari and Di Maio (2013) did not report on issues surrounding a discrepancy between measured resistivity values in the laboratory versus those found in the field, however, they did not directly measure suction and electrical properties at the same time, nor were their inverted field ERT images temperature corrected.

Crawford and Bryson (2018) applied a correction factor to convert inverted resistivities to matric potential, although such an approach would be difficult to fully justify in our case. Instead, we opted to apply our matric potential relationship directly to the temperature corrected ERT volumes; however, we often find that resistivity predicts the matric potential of the WMF to be effectively zero (Fig. 12), i.e., fully saturated. Nevertheless, converting electrical resistivity to a tangible geotechnical property is advantageous for conceptualising geophysical properties in terms of slope stability and communicating results to non-geophysicists. Our translation shows that the ERT resistivity distributions predict low suctions over the slip plane present within WMF and the monitoring area at Hollin Hill (Fig. 12 a-d). Though we show a relationship for the SSF in Fig. 9 our sample cavitated early in the experiment, so the results are unreliable and hence we focused on the WMF only.

A final consideration regarding petrophysical relationships is the apparent anisotropy of petrophysical relationships. We assume that the petrophysical relationships chosen to convert ERT volumes into moisture content and matric potential are representative. Modeling electrical anisotropy in rocks at the field scale is challenging. Some argue that resistivity should be modelled as a tensor (e.g. Bibby, 1977), and although solutions have been presented in the literature (Herwanger et al., 2004) they require well constrained regularisation to acquire a solution. To be fully sensitive to anisotropy some authors suggest 3D downhole borehole arrays are required (Greenhalgh et al., 2009), which are not present at Hollin Hill. Moreover, anisotropic inversion is not widely adopted in major inversion codes at the time of writing and developing a bespoke solution is well beyond the goals of this paper.

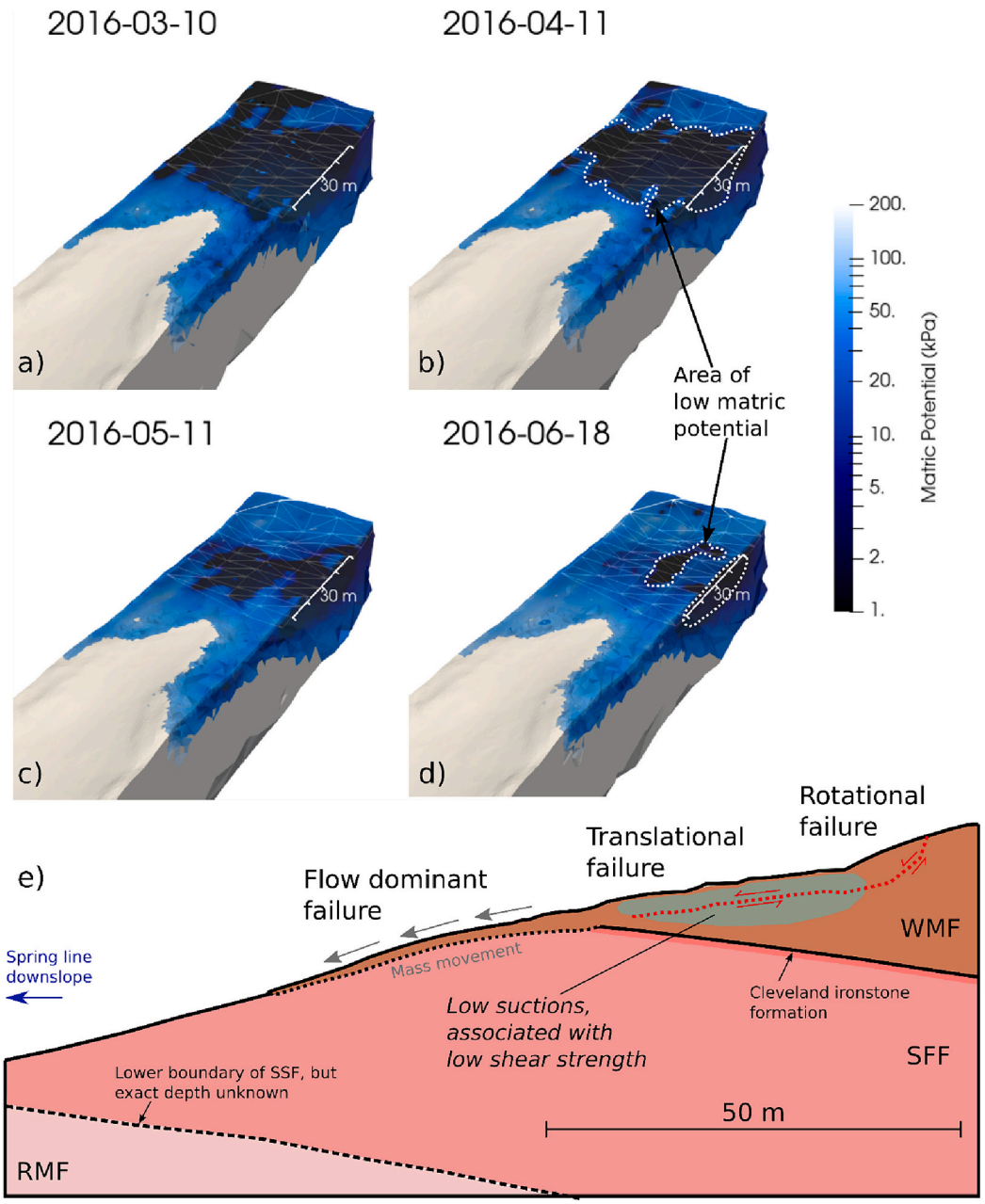

Fig. 12. a-d) Matric potential volumes derived from ERT processing and petrophysical calibration of Hollin Hill material around the development of the backscarp in April 2016. Slip surface is indicated with a white wireframe. Dates are presented in the format yyyy-mm-dd. e) Conceptual understanding of the hill slope, adapted and updated from Merritt et al. (2013), the line of the section is indicated in Fig. 1 b.

6. Hydromechanical interpretation

The model of the slip surface at Hollin Hill matches the surface expression of the observed backscarp; the uppermost part of the slope experiences rotational failure, which progresses into a translational failure downslope of the slip surface. Given the petrophysical relationship between electrical resistivity and matric potential, the ERT distribution is consistent with the low matric potentials (near zero) observed in the parts of the landslide that are actively failing (Fig. 3, Fig. 12). On the upper part of the slope low matric potentials are observed on top of the predicted slip surface (Fig. 12), which suggests disproportionately lower shear strengths in this part of the landslide. As other studies have suggested, the apparently low matric potential (and high moisture contents) in the mudstone unit could be attributed to a perched water level within the WMF (Gunn et al., 2013; Uhlemann et al., 2017). Although small matric potentials are not as frequently observed in the western flow lobe, which has experienced meter scale displacements throughout the monitoring period.

According to theories relating soil suction and shear strengths (Fredlund et al., 1978; Lu and Likos, 2006), small matric potentials correspond to low shear strengths and under a Mohr-Coulomb type failure regime would have a comparatively low factor of safety. This may explain the development of the rotational failure at the head of Hollin Hill, with a causal link between small matric potentials present in the months prior to and post movement (Fig. 12 b, d). Prior to movement low matric potentials are observed above the slip surface in the spring of 2016 (Fig. 12 a, b) and are reduced post movement during the summer (Fig. 12 c, d). The movement of flow lobes on the other hand are more difficult to explain with a Mohr-Coulomb failure criterion. Here plastic deformation is the main mechanism of movement and therefore

Atterberg limits (which define the plastic and liquid limits of clays) would be a more appropriate means of explaining the occurrence of failures.

By relating resistivity to hydromechanical states other than moisture content (or saturation), it is possible develop a direct means to assess the competency of the subsurface from a geotechnical engineering perspective. Note that Uhlemann et al. (2017) have previously shown GMC volumes derived from ERT at the HHLO. Here we conceptualise slope stability assessment using ERT as an indirect means to estimate the matric potential in unstable slopes, thereby adding some value to the geophysical images alone. We have validated our approach at the HHLO due to the availability of good ground truth information for model validation, hence the methods described here should be applicable to other moisture-driven landslides. Conversely, practitioners must appreciate caveats with the petrophysical relationships shown here. High plasticity clays (which are common in landslide prone areas) have properties such as variable porosity that make fitting classical petrophysical relationships challenging. Nevertheless, should appropriate petrophysical analysis take place alongside geoelectrical monitoring efforts, the methodologies described here could aid practitioners in landslide remediation strategies and early warning systems.

7. Conclusions

We describe an approach whereby the principal lithologies at the field site are identified in the geophysical imaging volume through clustering, which then informed the application of petrophysical relationships. To summarize, we found the following regarding petrophysical proxies:

- The porosity of the material at sample scale (cm) is a function of GMC. To acquire a reasonable fit for a modified Waxman- Smits relationship we require a variable porosity in our curve fitting process.
- A causal relationship between electrical resistivity and matric potential is observed and can be used to give an indication of matric potentials at Hollin Hill in the spatial and temporal domains.

Movement vectors for the electrodes at the field site (Hollin Hill) could be repurposed for estimating the geometry of the slip surface, which broadly agree with the in-field observations of the backscarp feature that first developed in 2016. Reconstructing a surface geometry allow for a joint interpretation of volumetric properties (e.g. resistivity and matric potential) with the location of the likely slip surface. We studied the porosity of Hollin Hill materials at various GMC levels via the SHRINKiT system (Hobbs et al., 2010) such that we can develop an Archie-type petrophysical transfer function. We measured electrical resistivity and matric potential simultaneously; despite a discrepancy between the range of resistivities observed in inverted images and those in HYPROP samples, this allowed us to translate ERT results into volumetric estimations of matric potential.

Comparisons of volumetric estimations of matric potential and slip location suggest that low matric potentials are concentrated above a translational slip surface towards the top of the slope before failure. The low matric potentials above the translational slip surface would account for lower shear strengths on that part of the landslide, hence causing movement downslope. We suggest that linking ERT to the hydromechanical properties of unsaturated materials of other unstable slopes has use for improving our understanding slope scale stability and likely failure areas. In an ERT time monitoring scenario, we also suggest that determining these appropriate resistivity relationships could enhance landslide early warning and remediation strategies for slopes comprising of expansive clays.

CRediT authorship contribution statement

James P. Boyd: Writing – original draft, Visualization, Software, Methodology, Investigation, Formal analysis, Data curation, Conceptualization. **Andrew Binley:** Writing – review & editing, Supervision, Funding acquisition, Conceptualization. **Paul Wilkinson:** Writing – review & editing, Supervision, Data curation, Conceptualization. **Jessica Holmes:** Methodology, Investigation, Formal analysis. **Edward Bruce:** Investigation, Formal analysis, Data curation. **Jonathan Chambers:** Writing – review & editing, Supervision, Funding acquisition, Conceptualization.

Declaration of competing interest

The authors declare the following financial interests/personal relationships which may be considered as potential competing interests:

James Boyd reports financial support and administrative support were provided by Natural Environment Research Council.

Data availability

Data will be made available on request.

Acknowledgements

We would like to thank Josie Gibson, Frances Standen and James Standen for their continued support over the years of monitoring Hollin Hill. This work is supported by the NERC doctoral training program, ENVISION (NE/L002604/1). We'd also like to thank two anonymous reviewers for their feedback improving this manuscript. This work is published with the permission of the Executive Director at the British Geological Survey.

References

Archie, G.E., 1947. Electrical resistivity an aid in core-analysis interpretation. AAPG Bull. 31, 350–366.

Aryal, A., Brooks, B.A., Reid, M.E., 2015. Landslide subsurface slip geometry inferred from 3-D surface displacement fields. Geophys. Res. Lett. 42, 1411–1417. https://doi.org/10.1002/2014GL062688.

Bibby, H.M., 1977. The apparent resistivity tensor. GEOPHYSICS 42, 1258–1261. https://doi.org/10.1190/1.1440791.

Binley, A., Slater, L., 2020. Resistivity and Induced Polarization: Theory and Applications to the Near-Surface Earth. Cambridge University Press, Cambridge.

Bishop, A.W., 1959. The principle of effective stress. Teknisk Ukeblad 39, 859–863.

Bishop, K.M., 1999. Determination of translational landslide slip surface depth using balanced cross sections. Environ. Eng. Geosci. 147–156.

Blanchy, G., Saneiyan, S., Boyd, J., McLachlan, P., Binley, A., 2019. In: University, L (Ed.), ResIPy, An Intuitive Open Source Software for Complex Geoelectrical Inversion/Modeling in 2D Space.

Booth, A.M., McCarley, J.C., Nelson, J., 2020. Multi-year, three-dimensional landslide surface deformation from repeat lidar and response to precipitation: Mill Gulch earthflow, California. Landslides 17, 1283–1296. https://doi.org/10.1007/s10346-020-01364-z.

Boyd, J., Chambers, J., Wilkinson, P., Peppa, M., Watlet, A., Kirkham, M., Jones, L., Swift, R., Meldrum, P., Uhlemann, S., 2021a. A linked geomorphological and geophysical modelling methodology applied to an active landslide. Landslides 1–16.

Boyd, J.P., Chambers, J., Wilkinson, P., Watlet, A., Holmes, J., Binley, A., 2021b. Linking field electrical resistivity measurements to pore suction and shear strength, for improved understanding of long term landslide stability. Sympos. Appl. Geophys. Eng. Environ. Probl. 2021, 155–159.

Camporese, M., Cassiani, G., Deiana, R., Salandin, P., Binley, A., 2015. Coupled and uncoupled hydrogeophysical inversions using ensemble Kalman filter assimilation of ERT-monitored tracer test data. Water Resour. Res. 51, 3277–3291. https://doi.org/10.1002/2014WR016017.

Cardoso, R., Dias, A.S., 2017. Study of the electrical resistivity of compacted kaolin based on water potential. Eng. Geol. 226, 1–11. https://doi.org/10.1016/j.enggeo.2017.04.007.

Carter, M., Bentley, S.P., 1985. The geometry of slip surfaces beneath landslides: predictions from surface measurements. Can. Geotech. J. 22, 234–238. https://doi.org/10.1139/t85-031.

Chambers, J., Gunn, D., Wilkinson, P., Meldrum, P., Haslam, E., Holyoake, S., Kirkham, M., Kuras, O., Merritt, A., Wragg, J., 2014. 4D electrical resistivity tomography monitoring of soil moisture dynamics in an operational railway embankment. Near Surf. Geophys. 12, 61–72.

Chambers, J.E., Wilkinson, P.B., Kuras, O., Ford, J.R., Gunn, D.A., Meldrum, P.I., Pennington, C.V.L., Weller, A.L., Hobbs, P.R.N., Ogilvy, R.D., 2011. Three-dimensional geophysical anatomy of an active landslide in Lias Group mudrocks, Cleveland Basin, UK. Geomorphology 125, 472–484. https://doi.org/10.1016/j.geomorph.2010.09.017.

Crawford, M.M., Bryson, L.S., 2018. Assessment of active landslides using field electrical measurements. Eng. Geol. 233, 146–159.

De Vita, P., Di Maio, R., Piegari, E., 2012. A study of the correlation between electrical resistivity and matric suction for unsaturated ash-fall pyroclastic soils in the Campania region (southern Italy). Environ. Earth Sci. 67, 787–798. https://doi.org/10.1007/s12665-012-1531-4.

Dixon, N., Spriggs, M., Meldrum, P., Ogilvy, R., Haslam, E., Chambers, J., 2010. Development of a Low Cost Acoustic Emission Early Warning System for Slope Instability.

Fischer, E.M., Knutti, R., 2016. Observed heavy precipitation increase confirms theory and early models. Nat. Clim. Chang. 6, 986–991. https://doi.org/10.1038/nclimate3110.

Fredlund, D., Morgenstern, N.R., Widger, R., 1978. The shear strength of unsaturated soils. Can. Geotech. J. 15, 313–321.

Fredlund, D.G., Xing, A., Fredlund, M.D., Barbour, S., 1996. The relationship of the unsaturated soil shear to the soil-water characteristic curve. Can. Geotech. J. 33, 440–448.

van Genuchten, M.T., 1980. A closed-form equation for predicting the hydraulic conductivity of unsaturated soils. Soil Sci. Soc. Am. J. 44, 892–898.

Gibson, A.D., Culshaw, M.G., Dashwood, C., Pennington, C.V.L., 2013. Landslide management in the UK—the problem of managing hazards in a 'low-risk' environment. Landslides 10, 599–610. https://doi.org/10.1007/s10346-012-0346-4.

Glover, P.W., Hole, M.J., Pous, J., 2000. A modified Archie's law for two conducting phases. Earth Planet. Sci. Lett. 180, 369–383.

Greenhalgh, S.A., Zhou, B., Greenhalgh, M., Marescot, L., Wiese, T., 2009. Explicit expressions for the Fréchet derivatives in 3D anisotropic resistivity inversion. Geophysics 74, F31–F43. https://doi.org/10.1190/1.3111114.

Gunn, D., Chambers, J., Hobbs, P., Ford, J., Wilkinson, P., Jenkins, G., Merritt, A., 2013. Rapid observations to guide the design of systems for long-term monitoring of a complex landslide in the Upper Lias clays of North Yorkshire, UK. Q. J. Eng. Geol. Hydrogeol. 46, 323–336.

Haque, U., da Silva, P.F., Devoli, G., Pilz, J., Zhao, B., Khaloua, A., Wilopo, W., Andersen, P., Lu, P., Lee, J., Yamamoto, T., Keellings, D., Wu, J.-H., Glass, G.E., 2019. The human cost of global warming: deadly landslides and their triggers (1995–2014). Sci. Total Environ. 682, 673–684. https://doi.org/10.1016/j.scitotenv.2019.03.415.

Hastings, W.K., 1970. Monte Carlo sampling methods using Markov chains and their applications. Biometrika 57, 97–109. https://doi.org/10.1093/biomet/57.1.97.

Hen-Jones, R.M., Hughes, P.N., Stirling, R.A., Glendinning, S., Chambers, J.E., Gunn, D. A., Cui, Y.J., 2017. Seasonal effects on geophysical–geotechnical relationships and their implications for electrical resistivity tomography monitoring of slopes. Acta Geotech. 12, 1159–1173. https://doi.org/10.1007/s11440-017-0523-7.

Herwanger, J.V., Pain, C.C., Binley, A., De Oliveira, C.R.E., Worthington, M.H., 2004. Anisotropic resistivity tomography. Geophys. J. Int. 158, 409–425. https://doi.org/10.1111/j.1365-246X.2004.02314.x.

Hobbs, P., Entwisle, D., Northmore, K., Sumbler, M., Jones, L., Kemp, S., Self, S., Butcher, A., Raines, M., Barron, M., 2005. The Engineering Geology of UK Rocks and Soils: The Lias Group. British Geological Survey IR/05/008, Nottingham, UK.

Hobbs, P., Jones, L., Roberts, P., Haslam, E., 2010. SHRINKiT: Automated Measurement of Shrinkage Limit for Clay Soils.

Holmes, J., Chambers, J., Meldrum, P., Wilkinson, P., Boyd, J., Williamson, P., Huntley, D., Sattler, K., Elwood, D., Sivakumar, V., Reeves, H., Donohue, S., 2020. Four-dimensional electrical resistivity tomography for continuous, near-real-time monitoring of a landslide affecting transport infrastructure in British Columbia, Canada. Near Surf. Geophys. 18, 337–351. https://doi.org/10.1002/nsg.12102.

Holmes, J., Chambers, J., Wilkinson, P., Meldrum, P., Cimpoiaşu, M., Boyd, J., Huntley, D., Williamson, P., Gunn, D., Dashwood, B., Whiteley, J., Watlet, A., Kirkham, M., Sattler, K., Elwood, D., Sivakumar, V., Donohue, S., 2022. Application of petrophysical relationships to electrical resistivity models for assessing the stability of a landslide in British Columbia, Canada. Eng. Geol. 301, 106613 https://doi.org/10.1016/j.enggeo.2022.106613.

Johnson, T.C., Versteeg, R.J., Ward, A., Day-Lewis, F.D., Revil, A., 2010. Improved hydrogeophysical characterization and monitoring through parallel modeling and inversion of time-domain resistivity andinduced-polarization data. Geophysics 75, WA27-WA41. https://doi.org/10.1190/1.3475513.

Johnson, T.C., Hammond, G.E., Chen, X., 2017. PFLOTRAN-E4D: A parallel open source PFLOTRAN module for simulating time-lapse electrical resistivity data. Comput. Geosci. 99, 72–80. https://doi.org/10.1016/j.cageo.2016.09.006.

Kuras, O., Pritchard, J.D., Meldrum, P.I., Chambers, J.E., Wilkinson, P.B., Ogilvy, R.D., Wealthall, G.P., 2009. Monitoring hydraulic processes with automated time-lapse electrical resistivity tomography (ALERT). Compt. Rendus Geosci. 341, 868–885. https://doi.org/10.1016/j.crte.2009.07.010.

Lu, N., Likos, W.J., 2006. Suction stress characteristic curve for unsaturated soil. J. Geotech. Geoenviron. Eng. 132, 131–142. https://doi.org/10.1061/(ASCE)1090-0241(2006)132:2(131).

Mboh, C.M., Huisman, J.A., Van Gaelen, N., Rings, J., Vereecken, H., 2012. Coupled hydrogeophysical inversion of electrical resistances and inflow measurements for topsoil hydraulic properties under constant head infiltration. Near Surf. Geophys. 10, 413–426. https://doi.org/10.3997/1873-0604.2012009.

Merritt, A.J., Chambers, J.E., Murphy, W., Wilkinson, P.B., West, L.J., Gunn, D.A., Meldrum, P.I., Kirkham, M., Dixon, N., 2013. 3D ground model development for an active landslide in Lias mudrocks using geophysical, remote sensing and geotechnical methods. Landslides 11, 537–550. https://doi.org/10.1007/s10346-013-0409-1.

Merritt, A.J., Chambers, J.E., Wilkinson, P.B., West, L.J., Murphy, W., Gunn, D., Uhlemann, S., 2016. Measurement and modelling of moisture—electrical resistivity relationship of fine-grained unsaturated soils and electrical anisotropy. J. Appl. Geophys. 124, 155–165. https://doi.org/10.1016/j.jappgeo.2015.11.005.

Merritt, A.J., Chambers, J.E., Murphy, W., Wilkinson, P.B., West, L.J., Uhlemann, S., Meldrum, P.I., Gunn, D., 2018. Landslide activation behaviour illuminated by electrical resistance monitoring. Earth Surf. Process. Landf. 43, 1321–1334.

Montaron, B., 2009. Connectivity Theory – A New Approach to Modeling Non-Archie Rocks. Petrophys. - SPWLA J. Form. Eval. Reserv. Descrip. 50.

Ogilvy, R., Meldrum, P., Kuras, O., Wilkinson, P., Chambers, J., Sen, M., Pulido-Bosch, A., Gisbert, J., Jorreto, S., Frances, I., 2009. Automated monitoring of coastal aquifers with electrical resistivity tomography. Near Surf. Geophys. 7, 367–376.

Ozturk, U., Bozzolan, E., Holcombe, E.A., Shukla, R., Pianosi, F., Wagener, T., 2022. How Climate Change and Unplanned Urban Sprawl Bring More Landslides. Nature Publishing Group.

Pedregosa, F., Varoquaux, G., Gramfort, A., Michel, V., Thirion, B., Grisel, O., Blondel, M., Prettenhofer, P., Weiss, R., Dubourg, V., 2011. Scikit-learn: machine learning in Python. J. Mach. Learn. Res. 12, 2825–2830.

Peng, X., Horn, R., 2005. Modeling soil shrinkage curve across a wide range of soil types. Soil Sci. Soc. Am. J. 69, 584–592. https://doi.org/10.2136/sssaj2004.0146.

Peppa, M.V., Mills, J.P., Moore, P., Miller, P.E., Chambers, J.E., 2019. Automated co-registration and calibration in SfM photogrammetry for landslide change detection. Earth Surf. Process. Landf. 44, 287–303.

Piegari, E., Di Maio, R., 2013. Estimating soil suction from electrical resistivity. Nat. Hazards Earth Syst. Sci. 13, 2369–2379. https://doi.org/10.5194/nhess-13-2369-2013.

Pleasants, M.S., Neves, F.D.A., Parsekian, A.D., Befus, K.M., Kelleners, T.J., 2022. Hydrogeophysical inversion of time-lapse ERT data to determine hillslope subsurface hydraulic properties. Water Resour. Res. 58, e2021WR031073 https://doi.org/10.1029/2021WR031073.

Saneiyan, S., Siegenthaler, E., Gimenez, D., Slater, L., 2022. Accuracy of Archie's law for clayey soils with high swelling capacity. SEG/AAPG Intern. Meet. Appl. Geosci. Energy. 3133–3137. https://doi.org/10.1190/image2022-3748322.1.

Tso, C.-H.M., Kuras, O., Wilkinson, P.B., Uhlemann, S., Chambers, J.E., Meldrum, P.I., Graham, J., Sherlock, E.F., Binley, A., 2017. Improved characterisation and modelling of measurement errors in electrical resistivity tomography (ERT) surveys. J. Appl. Geophys. 146, 103–119.

Tso, C.-H.M., Johnson, T.C., Song, X., Chen, X., Kuras, O., Wilkinson, P., Uhlemann, S., Chambers, J., Binley, A., 2020. Integrated hydrogeophysical modelling and data assimilation for geoelectrical leak detection. J. Contam. Hydrol. 234, 103679 https://doi.org/10.1016/j.jconhyd.2020.103679.

Uhlemann, S., Wilkinson, P.B., Chambers, J.E., Maurer, H., Merritt, A.J., Gunn, D.A., Meldrum, P.I., 2015. Interpolation of landslide movements to improve the accuracy of 4D geoelectrical monitoring. J. Appl. Geophys. 121, 93–105. https://doi.org/10.1016/j.jappgeo.2015.07.003.

Uhlemann, S., Hagedorn, S., Dashwood, B., Maurer, H., Gunn, D., Dijkstra, T., Chambers, J., 2016. Landslide characterization using P- and S-wave seismic refraction tomography — the importance of elastic moduli. J. Appl. Geophys. 134, 64–76. https://doi.org/10.1016/j.jappgeo.2016.08.014.

Uhlemann, S., Chambers, J., Wilkinson, P., Maurer, H., Merritt, A., Meldrum, P., Kuras, O., Gunn, D., Smith, A., Dijkstra, T., 2017. Four-dimensional imaging of moisture dynamics during landslide reactivation. J. Geophys. Res. Earth 122, 398–418. https://doi.org/10.1002/2016JF003983.

Vanapalli, S.K., Fredlund, D.G., Pufahl, D.E., Clifton, A.W., 1996. Model for the prediction of shear strength with respect to soil suction. Can. Geotech. J. 33, 379–392. https://doi.org/10.1139/t96-060.

Varnes, D.J., 1978. Slope Movement Types and Processes. Special Report, vol. 176, pp. 11–33.

Waxman, M.H., Smits, L., 1968. Electrical conductivities in oil-bearing shaly sands. Soc. Pet. Eng. J. 8, 107–122.

Whiteley, J., Chambers, J., Uhlemann, S., Wilkinson, P., Kendall, J., 2019. Geophysical monitoring of moisture-induced landslides: a review. Rev. Geophys. 57, 106–145.

Whiteley, J.S., Chambers, J.E., Uhlemann, S., Boyd, J., Cimpoiasu, M.O., Holmes, J.L., Inauen, C.M., Watlet, A., Hawley-Sibbett, L.R., Sujitapan, C., Swift, R.T., Kendall, J. M., 2020. Landslide monitoring using seismic refraction tomography – the importance of incorporating topographic variations. Eng. Geol. 268, 105525 https://doi.org/10.1016/j.enggeo.2020.105525.

Wilkinson, P.B., Chambers, J.E., Meldrum, P.I., Gunn, D.A., Ogilvy, R.D., Kuras, O., 2010. Predicting the movements of permanently installed electrodes on an active landslide using time-lapse geoelectrical resistivity data only. Geophys. J. Int. 183, 543–556. https://doi.org/10.1111/j.1365-246X.2010.04760.x.

van Woerden, J., Dijkstra, T.A., van Beek, L.P.H., Bogaard, T.A., 2014. The Role of Fissures in the Hydrology and Stability of the Hollin Hill Landslide. Masters Utrecht University.

Zreda, M., Desilets, D., Ferré, T.P.A., Scott, R.L., 2008. Measuring soil moisture content non-invasively at intermediate spatial scale using cosmic-ray neutrons. Geophys. Res. Lett. 35 https://doi.org/10.1029/2008GL035655.

Zreda, M., Shuttleworth, W.J., Zeng, X., Zweck, C., Desilets, D., Franz, T., Rosolem, R., 2012. COSMOS: the cosmic-ray soil moisture observing system. Hydrol. Earth Syst. Sci. 16, 4079–4099.